Intrinsic versus Practical Limits of Atmospheric Predictability and the Significance of the Butterfly Effect

Y. QIANG SUN AND FUQING ZHANG

Department of Meteorology, and Center for Advanced Data Assimilation and Predictability Techniques, The Pennsylvania State University, University Park, Pennsylvania

(Manuscript received 26 May 2015, in final form 16 November 2015)

ABSTRACT

Limits of intrinsic versus practical predictability are studied through examining multiscale error growth dynamics in idealized baroclinic waves with varying degrees of convective instabilities. In the dry experiment free of moist convection, error growth is controlled primarily by baroclinic instability under which forecast accuracy is inversely proportional to the amplitude of the baroclinically unstable initial-condition error (thus the prediction can be continuously improved without limit through reducing the initial error). Under the moist environment with strong convective instability, rapid upscale growth from moist convection leads to the forecast error being increasingly less sensitive to the scale and amplitude of the initial perturbations when the initial-error amplitude is getting smaller; these diminishing returns may ultimately impose a finite-time barrier to the forecast accuracy (limit of intrinsic predictability and the so-called ''butterfly effect''). However, if the initial perturbation is sufficiently large in scale and amplitude (as for most current-day operational models), the baroclinic growth of large-scale finite-amplitude initial error will control the forecast accuracy for both dry and moist baroclinic waves; forecast accuracy can be improved (thus the limit of practical predictability can be extended) through the reduction of initial-condition errors, especially those at larger scales. Regardless of the initial-perturbation scales and amplitude, the error spectrum will adjust toward the slope of the background flow. Inclusion of strong moist convection changes the mesoscale kinetic energy spectrum slope from -3 to $\sim -5/3$. This change further highlights the importance of convection and the relevance of the butterfly effect to both the intrinsic and practical limits of atmospheric predictability, especially at meso- and convective scales.

1. Introduction

Current-generation numerical weather prediction (NWP) models now are capable of routinely capturing the evolution of large-scale synoptic weather systems but remain challenged in forecasting meso- and convective-scale weather phenomena such as squall lines and tornadic thunderstorms. It is of great interest to assess the predictability of these mesoscale severe weather systems, what their predictability limits are, and how to improve our forecasts, particularly with respect to the amount and spatial distribution of the associated precipitation (Zhang et al. 2007). There are two types of predictability problems (Lorenz 1996; Melhauser and Zhang 2012): 1) practical predictability refers to the limit on atmospheric prediction using current optimal analysis procedures to derive the initial state with the best available atmospheric forecast model (Lorenz 1982) and 2) intrinsic predictability refers to the limit of prediction if the initial state is known nearly perfectly with an nearly perfect forecast model (Lorenz 1969; Zhang et al. 2007; Rotunno and Snyder 2008).

Practical predictability is limited by realistic uncertainties in the forecast model and initial conditions. These uncertainties can include the adequacy of observations (e.g., accuracy, spatial and temporal coverage, and usability), data assimilation procedures, and deficiencies in the forecast models (e.g., Lorenz 1996; Melhauser and Zhang 2012). The intrinsic predictability emphasizes that there will be a finite intrinsic limit of predictability for the atmosphere (as in any chaotic dynamic systems) even if the initial condition and forecast model are nearly perfect (e.g., Lorenz 1969; Zhang et al. 2003, 2007). This intrinsic predictability is demonstrated by the rapid ''upscale growth'' of the forecast error.

Corresponding author address: Professor Fuqing Zhang, Department of Meteorology, The Pennsylvania State University, 503 Walker Building, University Park, PA 16802.
E-mail: fzhang@psu.edu

DOI: 10.1175/JAS-D-15-0142.1

For a flow with a slope shallower than −3, idealized model studies show that this flow has a faster eddy turnover time at smaller scales. Thus, the growth rate of errors initially peaks at small scales and then, as the small-scale errors saturate, this peak shifts to larger scales with a smaller growth rate (Lorenz 1969; Rotunno and Snyder 2008). This type of ''upscale growth'' behavior is further demonstrated in Morss et al. (2009) with a quasigeostrophic model. The error growth behavior could also vary largely at different times or in different regions of interest, which leads to a flow-dependent predictability skill (Morss et al. 2009; Bei and Zhang 2014). In addition, using the NCAR Community Climate Model (version 3), Tribbia and Baumhefner (2004) confirms that upscale propagation of small-scale initial error is able to perturb the baroclinically unstable modes and results in the loss of predictability at global scales [refer also to Mapes et al. (2008)].

Zhang et al. (2007) proposed a multistage conceptual model for atmospheric predictability through diagnosing error growth between ''identical twin'' convection-permitting simulations of idealized moist baroclinic waves: 1) the initial convective growth stage, which begins with convective instability followed by rapid error saturation [$\sim O(1)$ h]; 2) the intermediate adjustment stage, during which error projects to balanced field [$\sim O(2\pi/f)$]; and 3) the large-scale growth stage where error grows with larger-scale baroclinic instability. This three-stage conceptual model is demonstrated to be effective in explaining the atmospheric predictability of a real-case study by Selz and Craig (2015a). In their high-resolution simulation of a warm-season weather event over Europe, Selz and Craig (2015a) showed that 60 h after perturbing their operational forecast model with negligible initial small-scale error, the large-scale 500-hPa geopotential height error induced by upscale error growth was about half the spread of the European Centre for Medium-Range Weather Forecasts (ECMWF) 6-h ensemble forecast. This result suggests that the upscale error growth plays a nonnegligible role in limiting the operational forecast skill and needs to be fully considered in numerical weather models. Rodwell et al. (2013) also related poor forecasts over Europe to high convective activities over North America a couple of days ahead, indicating that large uncertainties introduced by convection will amplify in scale and amplitude during the propagation over the Atlantic. In addition to midlatitude weather systems, the three-stage model is also found useful in explaining the predictability of tropical cyclones. In the study of four Indian Ocean cyclones, Taraphdar et al. (2014) found that the growth and saturation of error starts from small convective scales to intermediate mesoscale vortex or inertial gravity waves scales and ultimately influences the larger (system) scale of the tropical cyclones.

Recently, Durran and Gingrich (2014) argued that the initial relatively small large-scale error is more important than the upscale growth process of small-scale error proposed in Zhang et al. (2007). While they provided an interesting perspective, there are two important limitations in their study. First, their results are based on two winter storm cases during which convective instability is relatively weak. As atmospheric predictability is flow dependent, the result may well be different under different baroclinic and convective instability as shown in Tan et al. (2004). Second, Durran and Gingrich (2014) did not explicitly examine the intrinsic predictability of the two weather events in their study since initial-condition uncertainties in these two events, given by a particular initialization and data assimilation system of their model, are likely large in both in scale and amplitude [i.e., practical predictability of Lorenz (1982, 1996)]. The intrinsic predictability, on the other hand, refers to the limit of atmospheric predictability given infinitesimally small-scale, small-amplitude initial-condition errors (Lorenz 1969; Zhang et al. 2007).

As an extension of Zhang et al. (2007), this study explores both the intrinsic and practical aspects of atmospheric predictability through convection-permitting simulations of idealized moist baroclinic jet-front systems with initial-condition uncertainties at different scales and amplitudes. We will show that, for atmospheric predictability at the mesoscales, the role of moist convection and the upscale error growth starting from convective scales is critical for both the intrinsic and practical predictability. Section 2 introduces the model and methods used in the study. An overview of the simulated moist baroclinic systems is given in section 3. Section 4 explores the error evolution with initial perturbations of different scales. Their sensitivities to different amplitudes of initial perturbations are given in section 5. The dynamics of the error growth are explored in more details in section 6, with concluding remarks in section 7.

2. Methodology

a. Model configuration

The Advanced Research version of the Weather Research and Forecast Model (ARW version 3.5.1; Skamarock et al. 2008) is employed in this study following the configurations of Wei and Zhang (2014). The flow is confined to a periodic channel on an f plane ($f = 10^{-4}$), with a period of 4000 km in the zonal (x) direction and walls-separated 8000 km in the meridional (y) direction. There are 100 vertical layers with a model top at 20 km, which means roughly 200-m grid spacing in the vertical (z) direction. The horizontal grid spacing is 10 km, which is on the very edge of convection-permitting

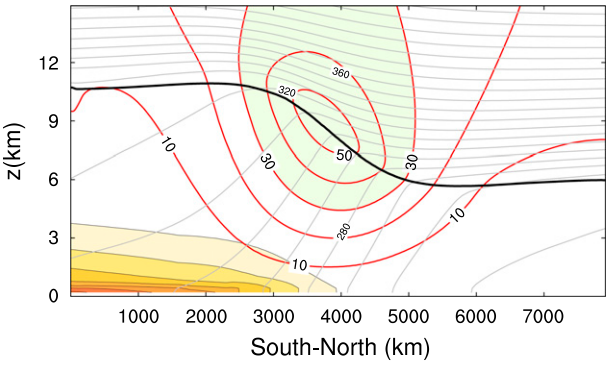

FIG. 1. Vertical cross section of the initial jet for zonal wind (red, every 10 m s^{-1}, >30 m s^{-1} light green shaded), potential temperature (gray, every 5 K), the tropopause denoted by dark line where the potential vorticity equals 1.5 PVU, and initial water vapor mixing ratio (color starts at 2 g kg^{-1} and is shaded every 2 g kg^{-1}).

resolutions and is likely to lead to some underestimation in the upscale error growth. With higher resolutions, the amplitude of the forecast error might change (Zhang et al. 2003, 2007). For example, Selz and Craig (2015b) found a factor of 3 amplitude differences in the 60-h difference total energy (DTE) error between a 2.8- and a 7-km "convection-permitting" simulation. Nevertheless, it is expected that a faster error growth with a higher resolution would follow similar physical processes (moist instability and convection) that may limit intrinsic predictability at the mesoscales and beyond.

The moist processes are parameterized using the Lin et al. (1983) microphysics scheme. The planetary boundary layer scheme of Hong and Pan (1996) is adopted here to handle the vertical diffusion in the simulation. The Monin–Obukhov similarity theory is used to parameterize the surface layer flux of heat and moisture. We also apply the Rayleigh damping scheme described in Klemp et al. (2008) to the vertical velocity in the uppermost 5 km of the model domain to minimize artificial wave reflections from the model top. To simplify the interpretation of the results, no cumulus parameterization is used and no radiation is considered.

b. *Initial conditions for the baroclinic wave simulations*

The initial jet profile is shown in Fig. 1. We use the same jet profile as that used in Zhang et al. (2007), which is derived through a simple 2D potential vorticity (PV) inversion (Davis and Emanuel 1991) method in the y–z plane. The prescribed PV distribution has constant value in both the troposphere [0.4 potential vorticity units (PVU, where 1 PVU = 10^{-6} K m^2 s^{-1} kg^{-1})] and stratosphere (4.0 PVU). The value of 1.5 PVU is used to define the location of tropopause, indicated by the thick black line in Fig. 1. More details of the jet profile can be found in Zhang et al. (2007) and Zhang (2004). This jet profile is then expanded along the x direction homogeneously. It is worth noting that, when using this jet as the initial condition, it went through an adjustment process and caused an artificial oscillation in the simulation, likely due to the interpolation across strong gradients. To remove this unwanted oscillation, we first run this jet profile for 35 h (around two times the inertial period) and then time average all the variables, and run this time-averaged field again. This procedure is repeated several times until the amplitude of the oscillating horizontal wind is reduced to the order of 0.001 m s^{-1}.

The initial relative humidity profile is prescribed with slightly smaller values than that in Zhang et al. (2007) (see appendix A). Figure 1 also shows the water vapor mixing ratio, which is very close to the observed values in the midlatitudes. This moisture profile will be noted as MOIST from now on. To test the sensitivity of the error growth to varying convective instabilities, two extra runs are also conducted, where the relative humidity is reduced to 50% of the original value or the diabatic heating is turned off completely, referred as RH50 and DRY, respectively.

The fastest-growing mode of the jet with a small amplitude (0.1 K for θ) is used to initiate the baroclinic wave cycle. This mode is computed using a method similar to that employed in Plougonven and Snyder (2007): first, we introduce a Gaussian noise to the jet and integrate the model for 3 days; the perturbation field is then rescaled to that of a smaller amplitude, which is added back to perturb the original jet again. This cycle is repeated five times for a total of 15-day simulation after which the normal mode of the perturbation fields is extracted to be the fastest-growing mode.

c. *Initial perturbations (errors) of the "identical twin experiments"*

Two types of perturbations are added to test the sensitivity of the short-range forecast error to initial-error distribution. Type one error is Gaussian white noise used in Zhang et al. (2007). This random noise with zero mean and a standard deviation of 0.2 K was added to the potential temperature fields (denoted as NOISE perturbation). Type two error is simply the filtered fastest-growing normal baroclinically unstable mode (amplitude 0.1 K for θ) in which only the long-wavelength part (large scale, wavelength > 1000 km) is retained. Note all the prognostic variables are perturbed accordingly to minimize initial imbalance. We will use LARGE to represent this perturbation in the following sections.

Various experiments are conducted to test all kinds of sensitivities related to the initial-perturbation

TABLE 1. All the experiments conducted in this study.

Moisture perturbation type	DRY	MOIST	RH50	FAKEDRY
LARGE	DRY_LARGE	MOIST_LARGE (L_H06, L_ H12, L_H18)	RH50_LARGE	FAKEDRY _LARGE
	DRY_LARGE10	MOIST_LARGE10		
	DRY_LARGE100	MOIST_LARGE100		
NOISE	DRY_NOISE	MOIST_NOISE (N_H06, N_H12, N_H18)	RH50_NOISE	FAKEDRY _NOISE
		MOIST_NOISE/10		

distribution and amplitude. A full list of all the experiments is listed in Table 1.

3. Overview of the baroclinic wave simulations

Before presenting our results on how the errors grow, a brief overview of the simulated baroclinic wave system is given here. Under the initial jet profile described above, the development and life cycle of the baroclinic wave follow a cyclonic behavior similar to the LC2 type defined in Thorncroft et al. (1993). Also note here, owing to the use of periodic boundary conditions in the zonal direction, the downstream development for both the baroclinic wave and error propagation could not be easily identified in the current study.

Figure 2 shows the simulated 500-hPa vertical vorticity of the baroclinic wave at days 5–8 under different moisture settings (that lead to different convective instability). A simple exponential amplification of the fastest-growing baroclinic mode dominates the evolution before day 5 (96 h). After day 8 (168 h), barotropic processes become important and the decay of the baroclinic wave starts to prevail (Simmons and Hoskins 1978). Consistent with previous studies on the LC2-type life cycle of baroclinic waves, the forward-tilted and broadening troughs are very clear in all three experiments. During the period between days 5 and 8, the large-scale vorticity structure is very similar in all the experiments, except that, in the moist runs, moist convection generates lots of local small-scale vorticity in the precipitation region. It is worth pointing that moist convection not only adds small-scale structures to the vorticity field but also promotes faster and stronger development of the large-scale flow. For example, the baroclinic trough becomes deeper and more curved in the MOIST run than in the DRY run. This can be more quantitatively illustrated by the time series of eddy kinetic energy (EKE) plotted in Fig. 3a. The EKE is defined as (Waite and Snyder 2013)

$$\mathrm{EKE} = \iiint \frac{1}{2}\rho(u'^2 + v'^2 + w'^2)\,dV \Big/ \iiint \rho\,dV, \quad (1)$$

where u', v', and w' are the perturbation fields after removing the zonal mean wind. Before day 5, the EKE of the DRY run and the MOIST run are very close. After the precipitation starts to form, the EKE of the MOIST run begins to grow at a higher growth rate. At day 8, the EKE of the MOIST and the RH50 runs are 52% and 24% higher than that of the DRY run, respectively. To ensure this higher EKE is not solely due to increment of the small-scale wave activity, the large-scale filtered EKE (wavelength $>$ 1000 km) is also shown. Again, the moist large-scale EKE is 51% higher than its counterpart in the dry run. Thus, it is very clear that EKE is dominated by its longer-wavelength baroclinic component. The meso- and small-scale components contribute less than 3% of the total EKE.

The precipitation rate of MOIST and RH50 is also shown in Fig. 3b. As we expected, precipitation in the MOIST run starts earlier and has a larger value throughout the simulation than RH50 because of a stronger convective instability in MOIST.

4. Intrinsic predictability: Forecast sensitivity to small-amplitude initial-condition errors

Considering the evolution of the baroclinic waves and the time when the precipitation starts, we choose to add the perturbations at 108 h (12 h after day 5) of the control baroclinic wave simulations described in the previous section. Two types of small-amplitude initial perturbations described in section 2 are added, the growth and evolution of which will be the focus of this section. As in Tan et al. (2004) and Zhang et al. (2007), the metric for examining the error is defined using the DTE:

$$\mathrm{DTE} = \frac{1}{2}\sum[(\delta u)^2 + (\delta v)^2 + \kappa(\delta T)^2], \quad (2)$$

where δu, δv, and δT are the difference winds and temperature fields, $\kappa = C_p/T_r$, C_p is the specific heat capacity, and T_r is the reference temperature of 270 K.

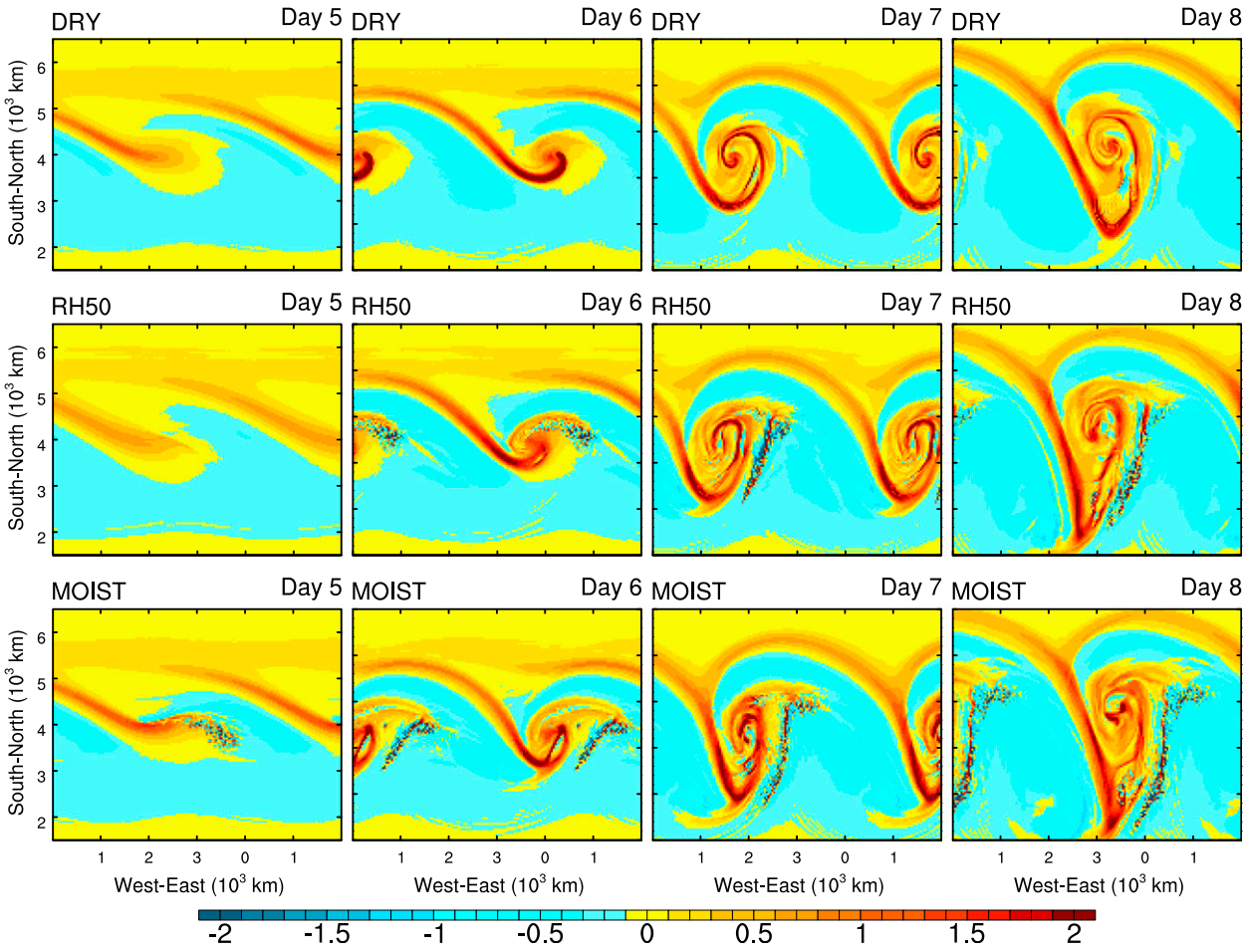

FIG. 2. Horizontal snapshots of the 500-hPa relative vorticity (10^{-4} s^{-1}) from (left to right) days 5 to 8 for the (top to bottom) control experiments of DRY, RH50, and MOIST. The distance between the tick marks on the axes is 1000 km. Regions within 1500 km of the southern and northern boundaries of the model domain are omitted.

a. Error growth from small-amplitude Gaussian white noises (NOISE)

Under the dry environment without convective instability, the initial perturbations grow solely through baroclinic instability. Since only a negligible part of the initial Gaussian white noise is projected onto the large-scale baroclinic mode, the overall growth in DTE from pure white noises is also weak in the DRY experiment. Instead, there is a noticeable decay of the initial error as a result of numerical model diffusion during the 36-h forecast period, as is shown in Fig. 4.

With the inclusion of moisture (and convective instability), however, the error growth behavior is drastically different (Fig. 4). Figure 5 shows the evolution of DTE and filtered large-scale difference sea level pressure in the MOIST_NOISE experiment overlaid with the simulated precipitation in the unperturbed simulation. As is expected, the evolution of initial error generally follows the three-stage model proposed by Zhang et al. (2007). In the first few hours, the error mainly grows through convective instability and is confined to the precipitation region. At later times, the error starts to project to large-scale balanced field while the unbalanced components of the error energy propagate away from the area of moist convection in the form of gravity waves and/or density currents, a hint of which can be seen in Fig. 5 (e.g., 18 h, on the edge of DTE field). The balanced components of the perturbations (error energy) eventually grow through large-scale baroclinic instability [see Zhang et al. (2007) for more details].

As for the vertical distribution of the error, Fig. 6 shows the contoured frequency by altitude diagram (CFAD) of the DTE in the MOIST_NOISE experiment. The largest DTE, contributed predominantly by the difference kinetic energy (DKE), lies at 8–10 km, the same location where the strongest wind (jet stream) lies in the background flow. Note that within less than 1 h,

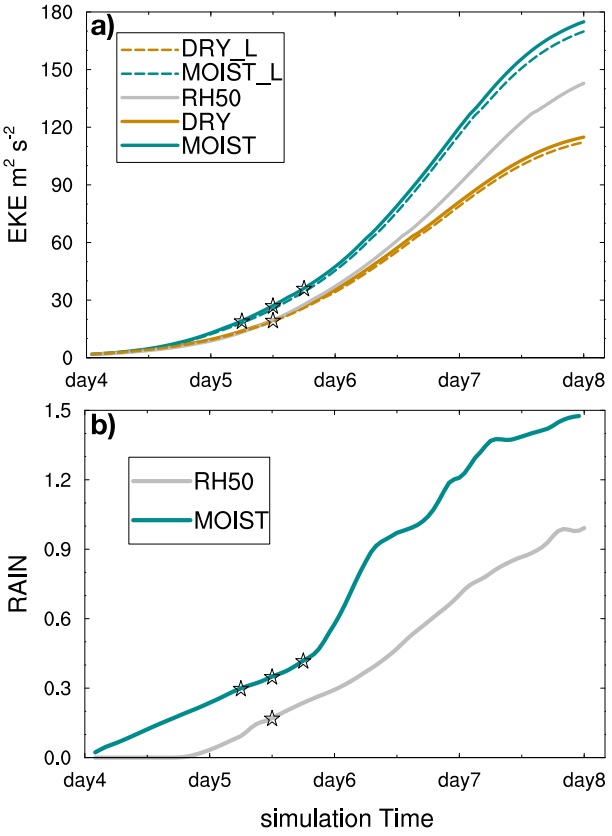

FIG. 3. (a) Time series of the simulated eddy kinetic energy per unit mass from different experiments. Dashed line shows the long-wave end of the eddy kinetic energy (wavelength > 1000 km). (b) Time series of the domain-averaged precipitation rate (mm every 12 h, averaged over 3-h intervals). The stars in both plots imply the time when the initial perturbations are added.

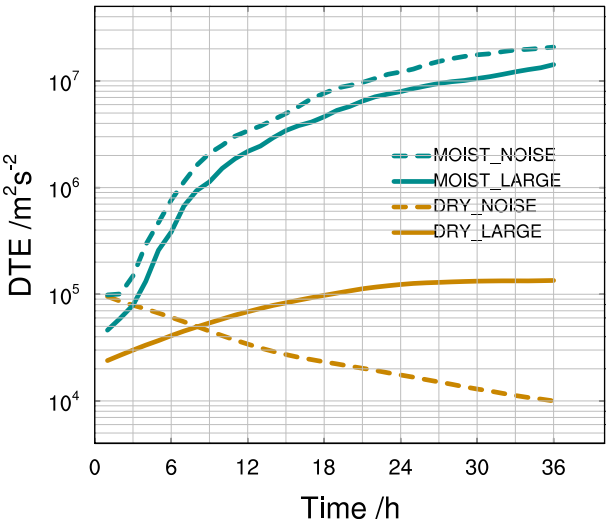

FIG. 4. Time series of the domain-integrated DTE (m^2 s^{-2}) for the NOISE (dashed) and LARGE (solid) experiments under DRY (gold) and MOIST (green) environment.

some strong DTE already shows up at around 9 km, implying a rapid conversion (and growth) from the error potential energy (only potential temperature is perturbed) to the error kinetic energy.

b. *Error growth for small-amplitude perturbations at the scale of fastest-growing mode (LARGE)*

The same analysis (as for the NOISE perturbation described above) is conducted for the LARGE case (Figs. 4 and 7) that is perturbed with small-amplitude initial-condition error at scales of the fastest-baroclinic-growing mode (wavelength > 1000 km). The evolution of DTE under dry environment follows an exponential growth with a growth rate similar to the growth of EKE in the control simulation. However, with the inclusion of moisture and convective instability, though initially the error growth at large scales shows some signature of the dry experiment (difference sea level pressure in Fig. 7), the total error growth is more similar to the MOIST_NOISE case consistent with the three-stage error growth conceptual model of Zhang et al. (2007) as also described above (Figs. 4 and 7), which is in strong contrast to the DRY_LARGE experiment without moisture. Note the final large-scale forecast error at 36 h in MOIST_LARGE experiment is even smaller than that of the MOIST_NOISE case. This evidence further verifies that the upscale error growth from convective scale dominates over the baroclinic error growth in this experiment when the initial-error amplitude is small, albeit large in scale.

It is worth noting that the baroclinic growth of the error nearly stalls after 30 h in the DRY_LARGE experiment because of the decrease of the baroclinic instability of the background large-scale flow (not shown). However, in the MOIST_LARGE experiment, the forecast error rapidly increases (especially in the large scale) as a result of precipitation at that time (Fig. 7). The increase of domain-integrated large-scale DTE at later forecast time (after 30 h) thus comes primarily through upscale propagation of error at smaller scales. While adding moisture itself will increase the baroclinic growth rate through reducing the static stability that can subsequently lead to an amplification of the large-scale error, this effect alone is too small to explain the difference between the MOIST_LARGE and DRY_LARGE experiments here.

c. *Experiments with initial perturbations added at different times of the baroclinic life cycle*

To further examine the robustness of the error growth characteristics discussed above, additional experiments are performed with initial perturbations added at different times of the baroclinic life cycle. In previous experiments, the initial perturbation is added at day 5

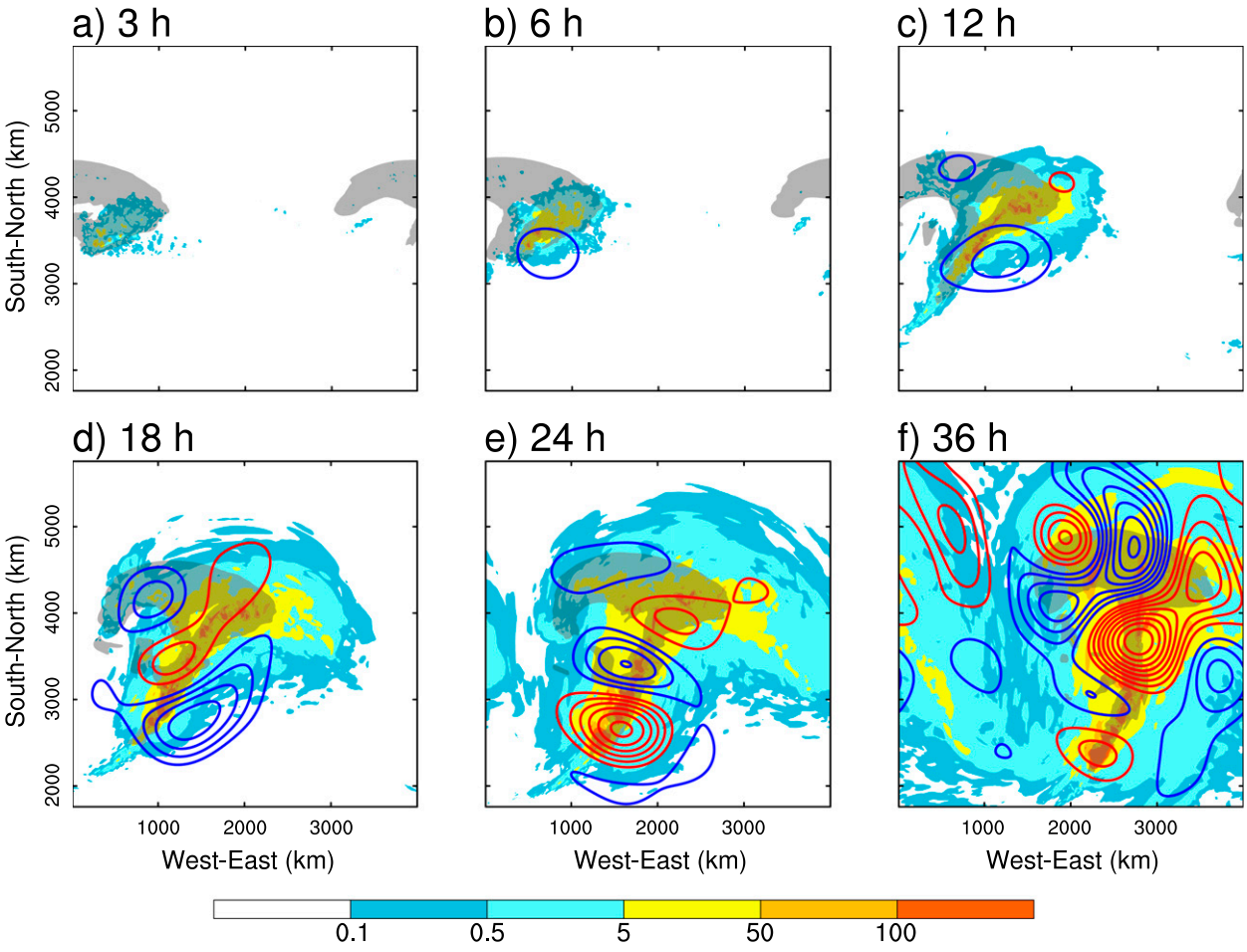

FIG. 5. Snapshots of column maxima of DTE ($m^2 s^{-2}$) for the MOIST_NOISE experiment valid at (a) 3, (b) 6, (c) 12, (d) 18, (e) 24, and (f) 36 h after the initial perturbations are added. The contours show the long-wave filtered sea level pressure difference (wavelength > 1000 km, every 5 Pa; red contour implies positive values and blue contour implies negative values. Gray shaded regions indicate where the precipitation rate is >0.1 mm h^{-1}.

at 12 h (108 h) of the control simulations, we refer to these two experiments with different perturbations as N_H12 and L_H12, respectively. We have also run similar experiments 6 h earlier and later at 6 and 18 h of day 5, which are noted here as N_H06, L_H06, N_H18, and L_H18, respectively. Thus, for each type of perturbation under the moist environment, we have three different perturbed runs. The list of all the experiments can also be found in Table 1.

Figure 8 shows the evolution of the domain-integrated DTE for all the three experiments for each type of perturbations. We can find that the DTE between short-range forecasts (e.g., at 12 h) is positively correlated to the precipitation rate. For example, the DTEs at 12 h in the H12 experiments are noticeably larger than that of the H06 experiments owing to stronger precipitation at later times (Fig. 3). After 20 h, the relationship between precipitation and the error growth is not as clear. Although the H12 and H18 experiments still have larger DTE compared to the H06 experiment, the difference between the H12 and H18 experiments becomes very small. Nevertheless, the error growth process in all the three experiments at different times is similar. We will thus focus on the H12 experiment for the analysis for MOIST_NOISE and MOIST_LARGE experiments if not stated otherwise.

Moreover, the error growth for both types of initial perturbations (MOIST_LARGE and MOIST_NOISE) is overall consistent with each other, all of which can be broadly described by the three-stage conceptual model of Zhang et al. (2007). In particular, the large-scale initial error in MOIST_LARGE acts primarily to perturb small scales in the region of moist convection, which makes little or no physical differences if the model is perturbed with the Gaussian white noises (NOISE). Additional experiments where we kept the LARGE perturbations only in the vicinity of moist convection (a circle

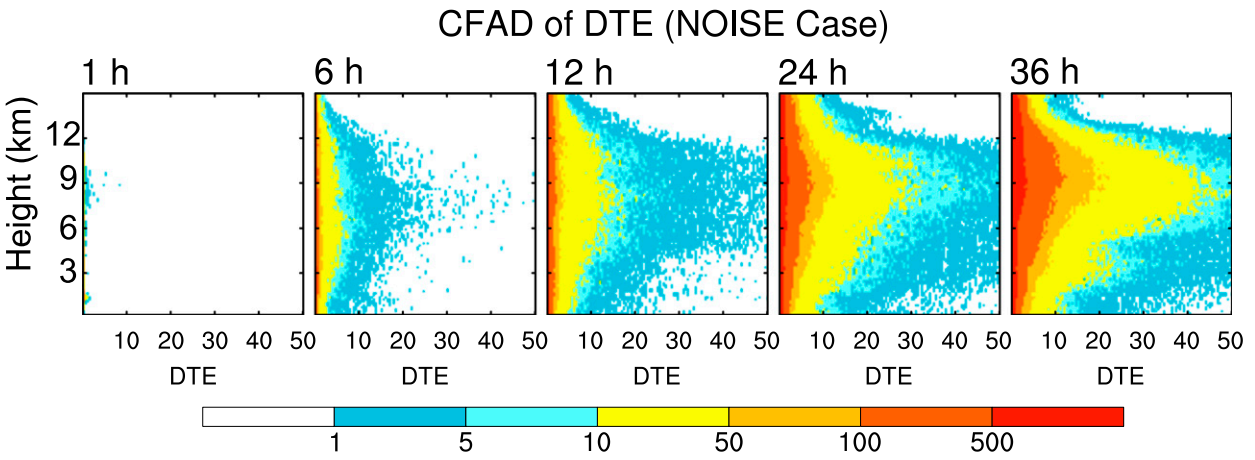

FIG. 6. Vertical distribution of DTE ($m^2 s^{-2}$) for the MOIST_NOISE experiment for (left to right) 1–36 h; shaded parts show the frequency (number of points) of DTE at a particular height.

with a radius of 200 km centered at the initial precipitation center) are also conducted (i.e., the initial-error scale is reduced by at least an order of magnitude) and the simulated DTEs are again quantitatively similar to the MOIST_NOISE and MOIST_LARGE experiments (except for the large-scale component of the DTE; not shown here). This high insensitivity of the convective-scale error growth to amplitude and structure of the perturbations is also demonstrated by Hohenegger and Schär (2007). In essence, the error energy for larger scales for the MOIST_LARGE experiments are not necessarily cascaded downscale [as found in Durran and Gingrich (2014)] but more likely grows from smaller-scale errors conditioned by the large-scale differences at the region of convective instability.

To summarize, consistent with previous studies of Zhang et al. (2007) and Selz and Craig (2015a), the experiments discussed in this section further support the three-stage conceptual model of Zhang et al. (2007) and strongly suggest that atmospheric predictability in the mesoscale might be intrinsically limited owing to chaotic dynamics of moist convection despite of being perturbed only by small-amplitude (unobservable) initial perturbations regardless of the initial-error scales.

5. Intrinsic versus practical predictability: Sensitivity to initial-error amplitude

Given that in the current-generation numerical weather prediction systems, the initial-condition errors can be both considerably large in scale and amplitude [as in Durran and Gingrich (2014)], this section examines the connections and differences between intrinsic and practical limits of atmospheric predictability through further exploring the error growth dynamics of the moist baroclinic jet–front systems with different initial-perturbation amplitudes (for both types of initial perturbations: LARGE and NOISE). These experiments are listed in Table 1. More specifically, the initial amplitude of the perturbations in experiments LARGE10 (LARGE100) is increased such that the initial domain-integrated DTE is 10 (100) times larger than that of LARGE (for both DRY and MOIST scenarios). The initial amplitude of the perturbations in experiment MOIST_NOISE/10 on the other hand is reduced such that the initial domain-integrated DTE is 1/10 that of MOIST_NOISE.

To help us better understand the error growth behavior at different scales, following Zhang et al. (2007) and with two-dimensional spectral decomposition, the domain-integrated DTEs for three characteristic horizontal-wavelength ranges (S: smaller scale, $L <$ 200 km; M: intermediate scale, 200 km $< L <$ 1000 km; L: larger scale $L >$ 1000 km) will be examined.

Under the DRY environment, the forecast errors for LARGE-type perturbations have a clear dependence on the amplitude of initial large-scale error that we added (Fig. 9). For example, the final domain-integrated DTE of DRY_LARGE10 (DRY_LARGE100) at 36 h is approximately 10 (100) times larger than the final DTE of DRY_LARGE. Moreover, this quasi-linear relationship holds true not only for the total DTE but also for DTE at different scales (Fig. 9). This set of DRY sensitivity experiments with LARGE-type initial perturbations demonstrates that error growth in dry baroclinic waves is primarily controlled by the exponential growth of the baroclinic mode due to the background baroclinic instability.

Under moist condition, to elucidate of the limit of intrinsic predictability, we further reduce the initial domain-integrated DTE of experiment MOIST_NOISE with the Gaussian white noise to one-tenth of its original value and mark this experiment as MOIST_NOISE/10. The forecast error in terms of DTE at 36 h

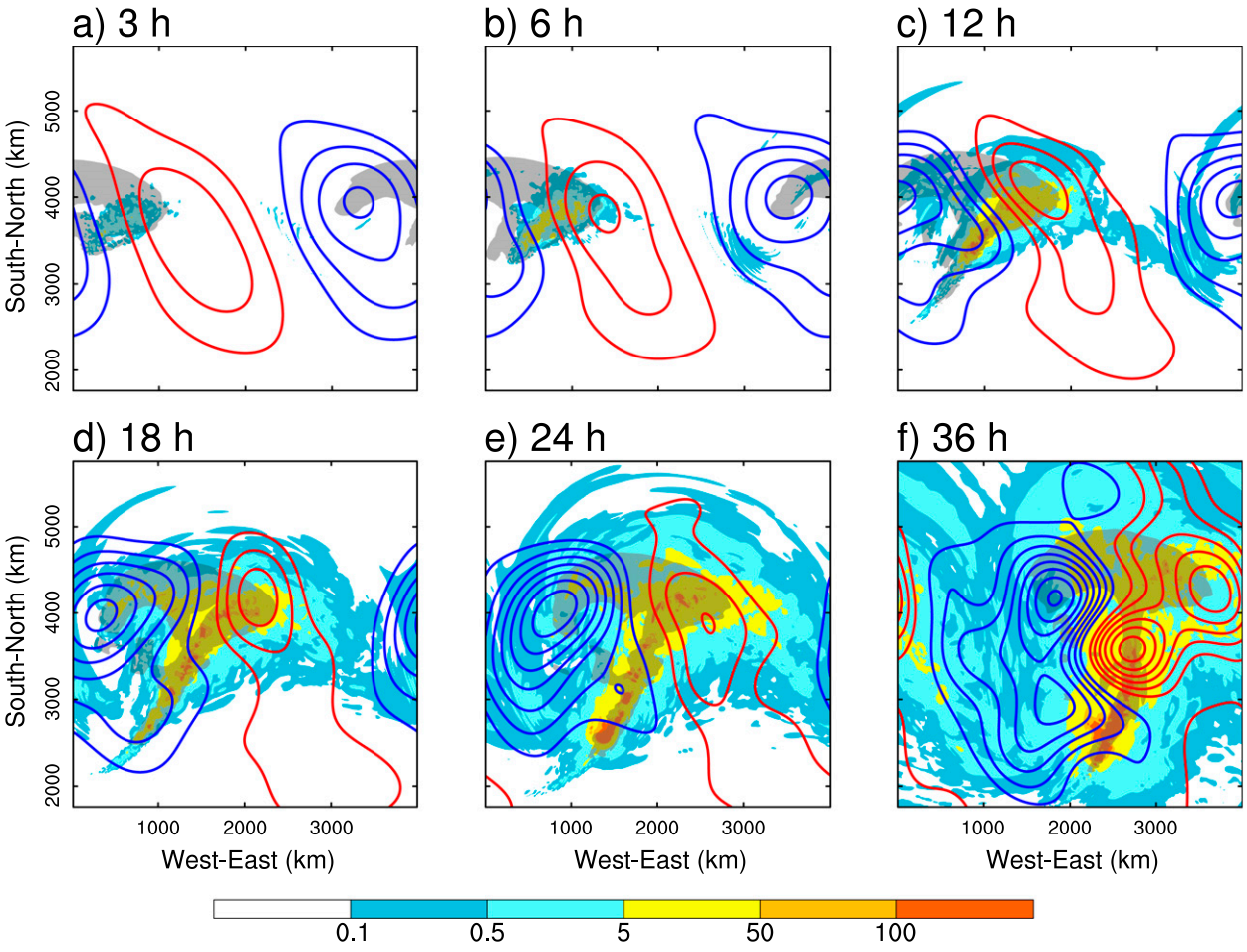

FIG. 7. As in Fig. 5, but for the MOIST_LARGE experiment.

for MOIST_NOISE/10 is almost the same as that of MOIST_NOISE—a strong indication of nonlinear error growth at the small scales. Further examination shows that, although starting at a smaller initial value, the small-scale error in the MOIST_NOISE/10 case grows much faster at the first few hours and catches up quickly with that in MOIST_NOISE. After the error at small scales saturated for both sets of experiments, the upscale error growth is similar in both MOIST_NOISE and MOIST_NOISE/10. This is also consistent with Hohenegger and Schär (2007). The strong nonlinear error growth at the small scales, and the insensitivity to the initial-error amplitude in these MOIST experiments, further demonstrates that atmospheric predictability can be intrinsically limited under the influence of moist convection, which means that our forecast accuracy will be limited no matter how small the initial-error amplitude is.

Nevertheless, given that the initial-condition errors in the weather prediction models at present are certainly not infinitesimally small either in scale and amplitude [as discussed in Durran and Gingrich (2014)], our attention is now turned to the limit of practical predictability through changing the (large scale) initial-perturbation amplitude in the MOIST_LARGE experiments. If we increase the initial DTE by a factor of 10 (MOIST_LARGE10), the final DTE at 36 h is only slightly larger ($\sim$1.5 $\times$) than in the MOIST_LARGE experiment. The final DTE of MOIST_LARGE10 is also very close to that of the NOISE experiment, including a close match for all of the three characteristic scale ranges (L, M, and S scales; Fig. 9). A further examination of the DTE evolution at the three characteristic scale ranges for MOIST_LARGE10 shows that, at the earlier simulation times before 20 h, the large-scale error generally follows the baroclinic growth in the DRY_LARGE case, while the small-scale error growth is similar to that of the MOIST_NOISE case. At later times, when the large-scale baroclinic growth slows down considerably (Fig. 9b; whereas the error begins to saturated at smaller scales), the error growth at the larger scales begins to come primarily from the upscale propagation of intermediate- and small-scale errors.

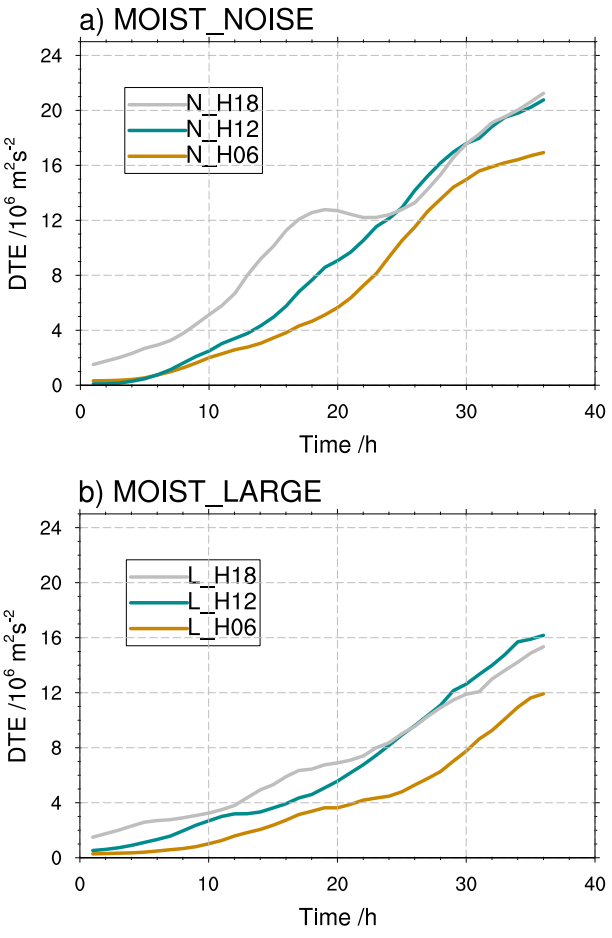

FIG. 8. Evolution of domain-integrated DTE ($m^2 s^{-2}$) for various (a) MOIST_NOISE and (b) MOIST_LARGE experiments perturbed at slightly different times (6, 12, and 18 h; see text for more details).

For the MOIST_LARGE100 experiment where the initial DTE is increased to 100 times that of MOIST_LARGE (with the maximum difference wind speed being around $2\,m\,s^{-1}$, comparable with the ensemble spread of current operational model), the error growth at the large scales now is similar to the DRY_LARGE100 experiment, although at later times (after 20 h) the large-scale error in MOIST_LARGE100 is slightly larger than that of DRY_LARGE100 likely as a result of upscale error growth from smaller scales in the MOIST_LARGE100 experiment. The total DTE at 36 h in MOIST_LARGE100 is more than twice higher than that of DRY_LARGE100, primarily because of a much more energetic small- and intermediate-scale error under the influence of moist convection. The error growth in the MOIST_LARGE100 experiment evolves more like that in Durran and Gingrich (2014), in the sense that the short-range large-scale error growth is hardly affected by the upscale growth of smaller-scale errors. In other words, if the initial-condition error is large in scale and considerably large in amplitude, as in the case of practical predictability, the considerably large-amplitude initial-condition error at the large scales is likely to be the most influential to the forecast quality. In this case, we can improve our forecast results through reducing the initial-condition error at the large scales, consistent with the findings of the recent study of Durran and Gingrich (2014), as well as Zhang et al. (2002), Bei and Zhang (2007), and many other authors.

However, even though Durran and Gingrich (2014) did not explore explicitly the growth of smaller-scale small-amplitude error as in the case of intrinsic predictability, they argued that the "butterfly effect" (nonlinear upscale error growth from small scales) could be easily overwhelmed by the growth from a relatively small-amplitude large-scale initial error. Their conclusion is not supported by our sensitivity experiments presented above. As in both of the MOIST_LARGE and MOIST_NOISE experiments (as well as MOIST_NOISE/10), regardless of the scales of the initial-condition error, if the amplitude of the initial perturbations is small, the short-range forecast is dominated by the upscale error growth from the small scales (the so-called butterfly effect), not necessarily cascading from the large-scale initial-condition error. In other words, there will be diminishing returns (increasingly smaller improvements) in the forecast accuracy through further reduction of the initial-condition error (as shown in the MOIST_NOISE/10 experiment), which is the essence of the butterfly effect.

Moreover, the drastic difference of the error growth and the final DTE amplitude between our DRY and MOIST experiments further illustrates the fundamental role of moist convection in limiting the intrinsic predictability. Sensitivity of the error growth to initial perturbations at different stages of the moist baroclinic life cycle also suggests that the stronger the convective instability, the faster error saturation at the smaller scales, and the more rapid upscale transfer of error to larger scales, as is shown in Selz and Craig (2015a). The sensitivity of error growth to the degree of convective instability can be further verified through the RH50 experiments perturbed with initial error of both LARGE and NOISE (Fig. 10), in which the background relative humidity of the initial baroclinic wave is reduced to 50% of the control moist experiment. Not surprisingly, with reduced moisture and convective instability, convection, and precipitation in RH50 are much delayed and weaker. Consequently, the forecast error in these RH50 experiments is much smaller than that in the corresponding MOIST experiments.

6. Error growth dynamics across different scales

In the previous two sections, we have shown the distinction between intrinsic and practical predictability. We

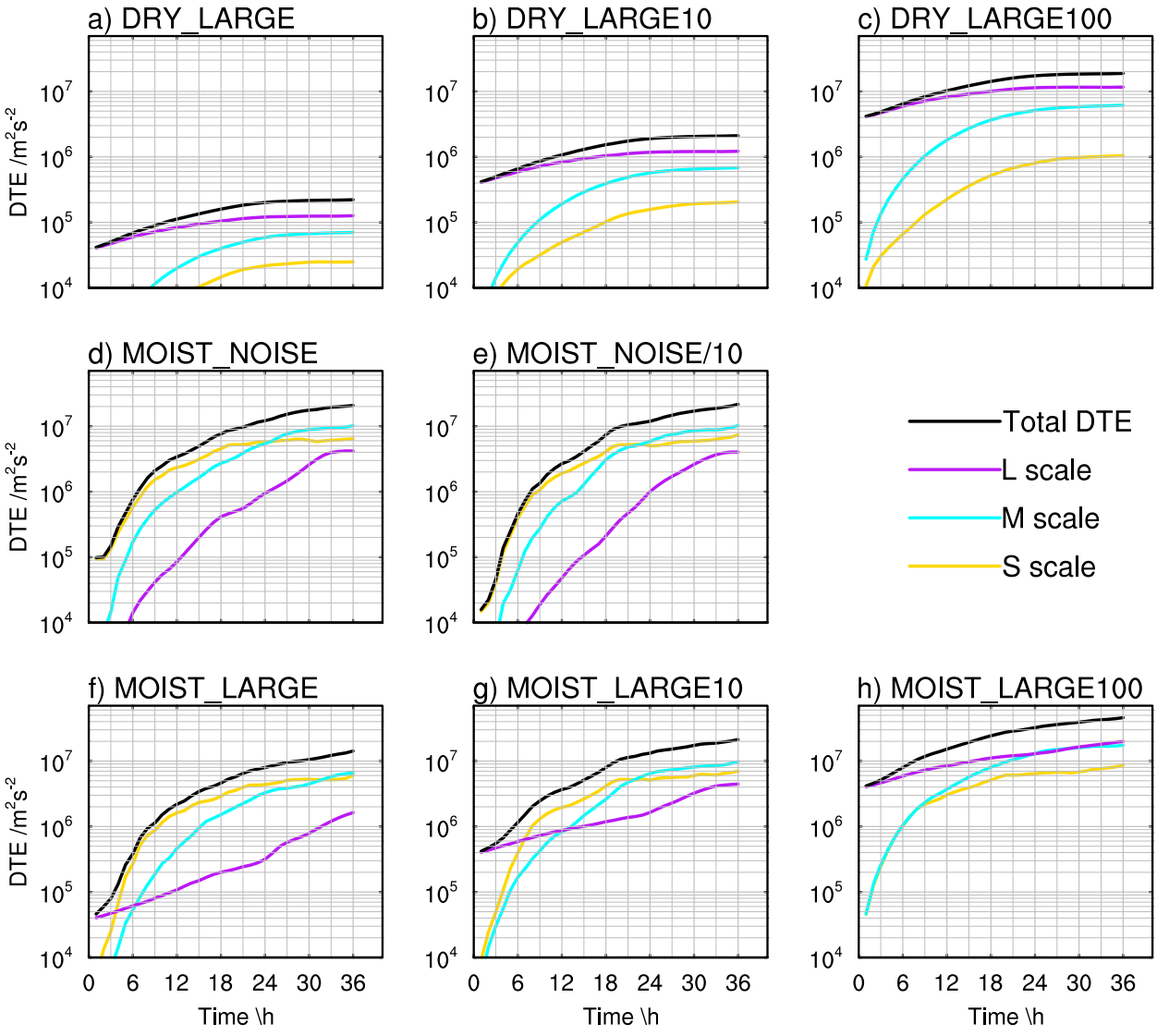

FIG. 9. Evolution of domain-integrated DTE ($m^2 s^{-2}$) for different wavelength scales (L: wavelength > 1000 km; M: 1000 > wavelength > 200 km; and S: 200 km > wavelength) in various experiments of different initial conditions. The experiment name implies the change of initial-error amplitude compared with its corresponding experiment (Table 1).

have also demonstrated that the upscale error growth from small scales under the influence of moist convection may critically limit the intrinsic predictability of the atmosphere at all scales. However, it remains uncertain whether the upscale error growth is still relevant under the practical predictability scenario where the initial error at the large scales is considerably large. We will investigate in more detail these questions in this section through diagnosing error growth and transfer across scales.

Figure 11 shows the evolution of power spectra for the domain-integrated difference total energy (DTE), which gives us a better sense of how the error grows at different scales. The spectral energy density of the full model state (24–36 h after perturbation) in control experiments is also plotted and multiplied by a factor of 2 (which does not change the slope), so that it represents the saturation level for the DTE. It is interesting to note that with the inclusion of moisture, the slope for the full model state transited from a steep −3 to a shallower close to $-5/3$[1] power law at a wavelength around 400 km. This transition is indeed consistent with the observational study of Nastrom and Gage (1985). As for the growth of the DTE, a clear cascading process could

[1] The calculated best-fit slope is −1.9 for wavelength between 80 and 400 km. Data with a wavelength smaller than 80 km are not used given than our current model horizontal grid spacing is 10 km.

be found under the DRY environment and the power spectra of the DTE grow at nearly the same rate at all scales. The DTE does not saturate until very late in the DRY_LARGE100 experiment. However, under the MOIST environment, the DTE at small scales quickly saturate after the perturbation is added regardless of the initial amplitude of the perturbation (refer to MOIST_LARGE and MOIST_LARGE100).

For the practical predictability scenario with considerably large initial-condition error at the large scale (MOIST_LARGE100), the upscale growth of error from smaller scales becomes less evident. Similar to the real-data case of Durran and Gingrich (2014), the error shows a more uniform growth over all the scales (especially for larger scales; see Fig. 11d). This is also similar to the DRY_LARGE100 experiment (Fig. 11b), except that in the MOIST_LARGE100 case, the spectral slope of for small-scale error with a wavelength smaller than 400 km flattens to approximately −5/3 rather than −3.

Since there are inherent two-way interactions among different scales, it is indeed very difficult to completely separate the upscale growth of the convective-scale error and the error growth within the large scale itself. To help us further understand if the upscale growth plays a role in the change of the error spectral slope, a budget analysis for DKE (difference kinetic energy) at the three characteristic scale ranges (L, M, and S) is performed. The equation for DKE budget at large scale can be written as

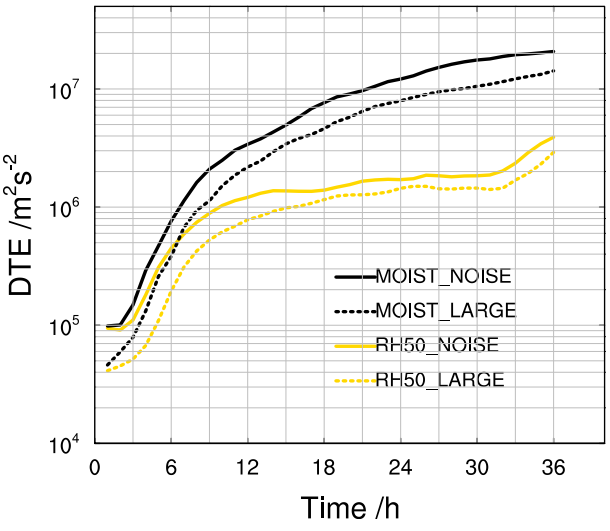

FIG. 10. Evolution of domain-integrated DTE ($m^2 s^{-2}$) under different moisture environments. RH50 here means the initial relative humidity (RH) is reduced by half to that of the moist case.

$$\frac{\partial}{\partial t}(\mathrm{DKE})_L = \left[-\overline{\rho}(\delta u)_L \delta\left(\mathbf{u}\cdot\nabla_h u + w\frac{\partial u}{\partial z}\right)_L - \overline{\rho}(\delta v)_L \delta\left(\mathbf{u}\cdot\nabla_h v + w\frac{\partial v}{\partial z}\right)_L\right] + \left[-\overline{\rho}(\delta u)_L \delta\left(\frac{1}{\rho}\frac{\partial p'}{\partial x}\right)_L - \overline{\rho}(\delta v)_L \delta\left(\frac{1}{\rho}\frac{\partial p'}{\partial y}\right)_L\right] + (\mathrm{Damping})_L, \quad (3)$$

where $(\mathrm{DKE})_L = (1/2)\overline{\rho}[(\delta u)_L^2 + (\delta v)_L^2]$. (The derivation for this equation can be found at appendix B.) For intermediate and small scales, the equations are essentially the same except that the subscripts of the terms are changed to M or S. The two terms in the first brackets on the right-hand side of this equation represent the nonlinear advection term (referred to as ADV), which is responsible for the redistribution of the error across different scales. The terms in the second brackets represent the pressure term, which mainly represents the conversion between difference potential energy and difference kinetic energy (see appendix C).

The results of the DKE budget analysis for three different scales are given in Fig. 12. Under the dry environment, there is a clear downscale error transfer for DRY_LARGE100 (top panel of Fig. 12), where the peak of large-scale error growth shows first, followed then by the peak of the medium scale; the peak of small-scale error growth comes last. It is also worth pointing out that, for this downscale error transfer, the ADV term leads the pressure term and dominates the error growth for the medium and the small scales, which is consistent with the hypothesis that error first propagates to smaller scales through the nonlinear advection term.

The MOIST_NOISE and MOIST_LARGE experiments, on the other hand, demonstrate an apparent upscale error growth picture as seen from the budget analysis. The error growth first is evident only at the small scales; it then gradually expands to the medium and the large scales. The pressure term and the ADV term contribute equally at all the scales. The ADV term is actually enhanced by the pressure term (through the buoyancy flux). If we turn off the latent heating, not only the pressure term but also the ADV terms will immediately drop to near zero.

For the MOIST_LARGE100 experiment, both the downscale and upscale error growth processes are present. At the large scale, the error grows similarly to the corresponding dry experiment in the first 20 h, while

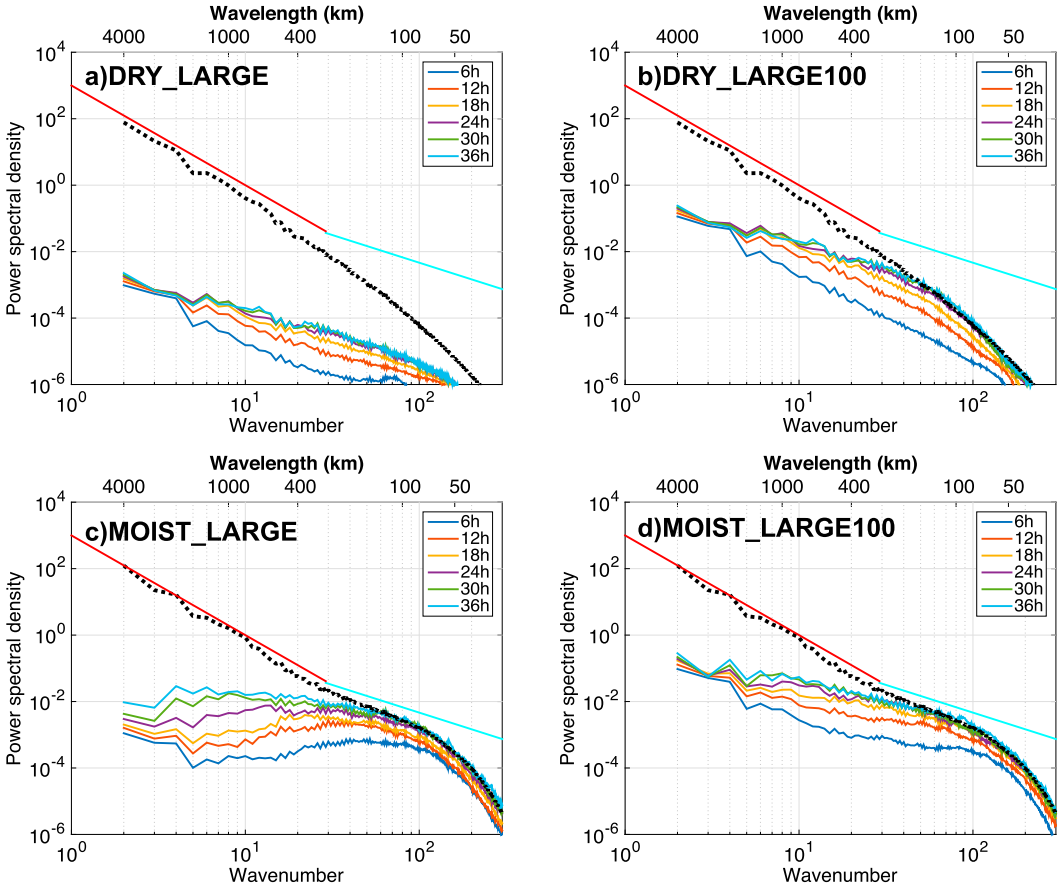

FIG. 11. Evolution of the DTE ($m^2 s^{-2}$) spectra every 6 h after different initial perturbations are added for 6–36 h: (a) DRY_LARGE, (b) DRY_LARGE100, (c) MOIST_LARGE, and (d) MOIST_LARGE100 experiments. Dotted lines show the spectra of the full-state background flow in the control experiment, averaged between 24 and 36 h after the perturbation. The red and blue lines show the reference line for −3 and −5/3 power laws, respectively.

at the small scale, the upscale growth is apparent, with the pressure term and ADV term contributing equally to the growth. For the intermediate scale in this case, because of the influence of downscale propagation of the large-scale initial error, the ADV term plays a slightly bigger role than the pressure term. Nonetheless, the pressure term is also very important for the intermediate-scale error growth, especially at later simulation times when the background baroclinic growth is weakened. The upscale propagation effect can be convincingly demonstrated through the error growth budget for the large scale after 20 h: the growth of DKE for the large scale in the MOIST_LARGE100 case continues while the growth at the large scale diminishes in the corresponding DRY_LARGE100 experiment as a result of weakening of the background baroclinic growth.

Moreover, with the energy spectra flattened to a slope close to −5/3 in the moist environment, the mesoscale energy spectra (wavelength < 400 km) increase dramatically in the MOIST case, the forecast short-range error (36 h) for intermediate and small scales in the MOIST_LARGE experiment is more than 3 times larger than that in the corresponding DRY_LARGE100 experiment (Fig. 9). Thus, the dominant error source for the mesoscale is due to convection. Failure to predict the location and/or the strength of the convection characters would likely lead to a more inaccurate mesoscale forecast. Hence the weak sensitivity of the convective cells to initial perturbation and the upscale growth not only leads to less intrinsically predictability but likely also plays a substantial role in limiting the practical predictability at mesoscale. To further verify this, the power spectrum of the latent heating forcing difference, which shows the scale of moist forcing (buoyance production), is plotted in Fig. 13 for both the MOIST_NOISE and the MOIST_LARGE100 experiments. This forcing at different scales can be defined as in Eq. (7) of Waite and Snyder (2013):

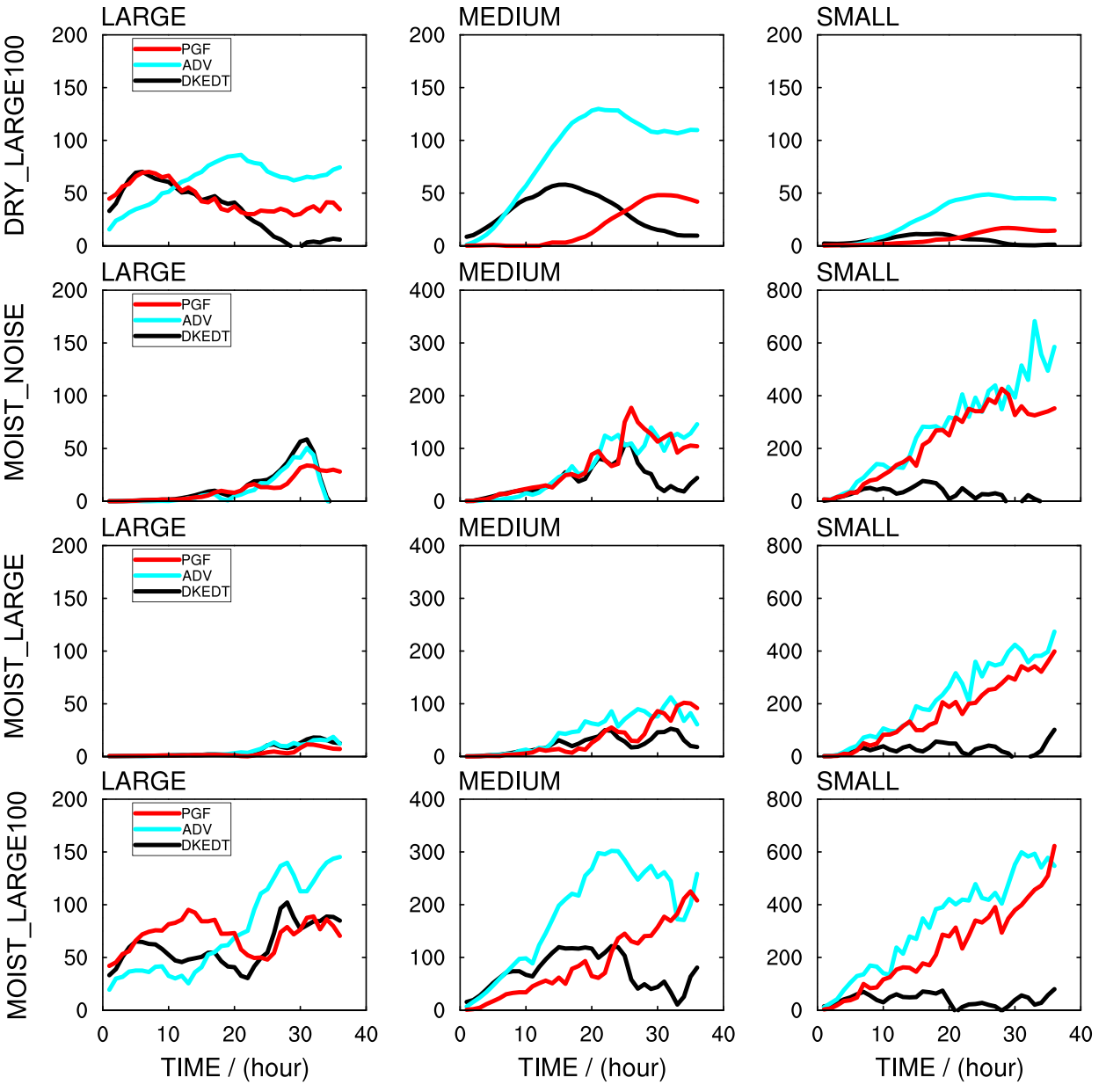

FIG. 12. Time series of budget calculations for the sources and sinks of the DTE [dDKE/dt, kg m^2 s^{-3}, Eq. (3), values are integrated over the domain] at (left to right) different wavelengths within (top to bottom) DRY_LARGE100, MOIST_NOISE, MOIST_LARGE, and MOIST_LARGE100 experiments. The cyan, red, and black lines represent the contribution of the advection and pressure terms, and the actual increment of DKE after diffusion and damping, respectively. Note that the DRY_LARGE100 experiment has different vertical scales from the others.

$$F(k) = \frac{1}{2}\delta[\hat{\theta}^*(k)]\delta[\hat{H}(k)] + \text{c. c.},$$

where H is the potential temperature tendency due to moist physics. A 12-h time average is used in Fig. 13, where the semilog axis is considered to preserve the area. The latent heating forcing shows no significant difference between the MOIST_NOISE and the MOIST_LARGE100 experiments. At first, this forcing acts mainly on the small scales (wavelength $\sim$ 100 km). Later, it expands to larger scales, with the peak spectral power of the forcing remaining at the meso- and smaller scales. The similarity of these two experiments further suggests that experiment MOIST_LARGE100 (under the practical predictability scenario) does not bring more (additional) forcing through buoyancy production than MOIST_NOISE

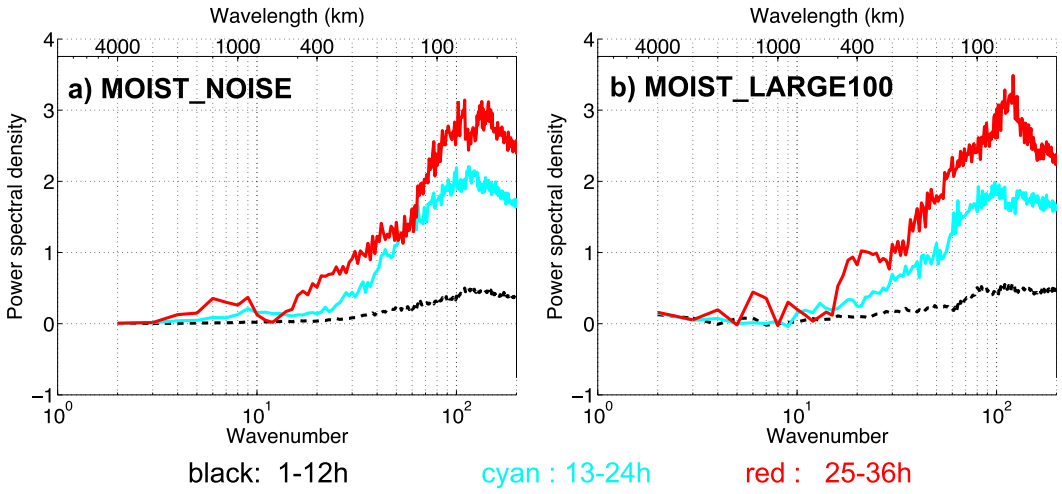

FIG. 13. Difference buoyancy production spectra for experiments (a) MOIST_NOISE and (b) MOIST_LARGE100 environment. The black dashed, cyan, and red lines show time average over 1–12, 13–24, and 25–36 h, respectively. The buoyancy production is multiplied by the wavenumber to preserve the area on a log-linear plot.

(under the intrinsic predictability scenario). In other words, the primary role of the initial large-scale perturbation in this MOIST_LARGE100 experiment is through direct projection of the initial difference to trigger the error growth, saturation, and upscale transfer of small-scale moist convection that is similar to the MOIST_NOISE experiment, not necessarily through the downscale error cascade from the initial large-scale perturbation.

7. Concluding remarks

Through a series of ''identical twin experiments'' with the Weather Research and Forecast (WRF) Model by adding initial-condition errors of different scales and amplitudes, this study explores the limits of both intrinsic and practical predictability and the multiscale error growth dynamics of the baroclinic jet-front systems with varying degree of convective instabilities.

In the dry experiments free of moist convection (and the ''FAKEDRY'' experiments that suppress convection through turnoff of diabatic heating), only the baroclinic growth of the large-scale perturbation can be found in the 36-h short-range forecast. The forecast error under the dry environment has a quasi-linear dependence on the amplitude of the initial large-scale perturbation. This suggests that the forecast accuracy can be continuously improved through reducing the initial condition and thus predictability for the dry baroclinic waves can be continuously improved without an apparent limit at the synoptic time scales if the forecast model and the initial conditions are nearly perfect (though other sources of smaller-scale instabilities such as boundary layer turbulence and shear instability that are not studied here may also trigger upscale error growth that may eventually limit the intrinsic predictability).

The limits of both intrinsic and practical predictability are found to be drastically different under the moist environment with strong convective instability. The rapid upscale error growth from moist convection will lead to the forecast error being increasingly less sensitive to the scale and amplitude of the initial perturbations when the initial-error amplitude is sufficiently small, as characterized in the multistage error growth conceptual model of Zhang et al. (2007). Because of the strong nonlinear upscale error growth from moist convection, there will be diminishing returns (increasing smaller improvements) in the forecast accuracy through further reducing the initial-condition error—a key indicator of limit of intrinsic predictability (Lorenz 1969; Rotunno and Snyder 2008; Palmer et al. 2014). In other words, the distance between the practical and intrinsic predictability limits become smaller and smaller as the initial-condition accuracy continues to improve. On the other hand, when the initial perturbations are sufficiently large in scale and amplitude, as for most current-day operational models, the baroclinic growth of large-scale finite-amplitude initial error will play a more dominant role in the forecast accuracy at all scales for both dry and moist baroclinic waves. The forecast accuracy can be further improved (and thus the limit of practical predictability can be extended) through reduction of initial-condition errors, especially those at

larger scales. Even in this case, the upscale error growth from convective instability under the moist environment could still be crucial for predictability of mesoscale processes. In addition, as is pointed out in Rodwell et al. (2013), the upscale error growth might also become relevant for larger scales at longer forecast lead times, although its importance may be flow dependent. Furthermore, an insufficiently simulated upscale error growth may well be one of the reasons for the underdispersion issue in nowadays ensemble predictions. All of these studies imply the practical importance of the butterfly effect—the rapid upscale error growth from moist convection that has an intrinsic predictability limit.

It is also worth noting here that, if we consider the life cycle of the baroclinic wave, the results showed above will have dependence on the development stage of the baroclinic system. For example, to focus on the convective instability, the forecast experiments in this paper start from day 5 when the baroclinic system has been already in a mature stage and tended to cease an exponential growth as shown in Fig. 2. Hence, the period during which the baroclinic wave grows exponentially is quite short of $O(1)$ day (Fig. 3), as evident in the error growth shown in Fig. 9, which indicates that the large-scale error ceases the exponential growth after about 1 day for the DRY_LARGE experiment. As shown in Zhu and Thorpe (2006), the large-scale error usually sustains exponential growth during a period of at least 77 h when the basic state is specified by an initial developing stage of the baroclinic system. Hence, we might underestimate the error growth of large-scale motions associated with the inherent baroclinic instability in the current study. The underestimation might be related to the result on the relative importance of convective instability and the subsequent upscale error growth. Similar caveat is also noted in Palmer et al. (2014) by conducting forecasts experiments based on the surface quasigeostrophic equation from different initial conditions. They remarked on the intermittent characteristic of the butterfly effect and the flow-dependent nature of the large-scale forecast sensitivity to small-scale initial error. Thus, the crucial role of convective instability in the large-scale error growth discussed in the current study might also depend strongly on the prescribed initial flow conditions.

The connection and difference between practical and intrinsic predictability was also succinctly illustrated in the schematic diagram of Fig. 18 in Melhauser and Zhang (2012), which is abstracted from the mesoscale predictability study of a strong warm-season bow echo and squall-line event. We believe this conceptual diagram can be generalized to the current study of idealized moist baroclinic waves, as well as to our studies of winter snowstorms (Zhang et al. 2002, 2003), springtime tornadic thunderstorms (Zhang et al. 2015, 2016), warm-season flooding (Zhang et al. 2006; Bei and Zhang 2007), as well as hurricanes and tropical cyclones (Zhang and Sippel 2009; Zhang and Tao 2013; Tao and Zhang 2014, 2015).

The predictability behavior is closely linked to the flow's kinetic energy spectrum. As mentioned in the introduction, previous studies have already shown the existence of a predictability limit with a shallower than -3 slope (Rotunno and Snyder 2008). Under the moist environment with the inclusion of strong moist instability, the slope of the background kinetic energy spectrum decreases from -3 to $-5/3$. This transition of the spectral slope emphasizes the importance of convection to both the intrinsic and practical limit of mesoscale predictability within the moist baroclinic jet-front systems. However, the exact reason(s) for this transition is beyond the scope of the current study. This change may be due to the strong turbulent motions that are induced by moist convection that becomes more homogeneous and isotropic and/or much stronger gravity waves induced by convection [as shown in Wei and Zhang (2014)]. Past theoretical studies suggest that both three-dimensional turbulent motion and the linear gravity waves could have a slope of $-5/3$ (e.g., Vallis 2006). However, neither of these two hypotheses are ready to explain the transition scale at a horizontal wavelength around 500 km, which is found in our simulations as well as in observational studies (e.g., Nastrom and Gage 1985). Recently, Callies et al. (2014) utilized a modified Helmholtz decomposition method to process the observation data by the flight through which they claimed that the small-scale fluctuations are dominated by gravity wave activity. If this is the case, since linear inertia gravity waves do not propagate error upscale in the same way as the vortical turbulent flows discussed by Lorenz (1969), the forecast times of weather systems could potentially be extended considerably. We plan to conduct further research on this topic. Nonetheless, the change of the kinetic energy spectrum slope is clearly due to moist convection and emphasizes the importance of convection on the limit of mesoscale predictability.

Acknowledgments. We are very grateful to Dr. Shuguang Wang and Dr. Junhong Wei for help setting up the experiments. The authors benefits greatly from discussions with Dr. Rich Rotunno, who also suggested the use of spectral decomposition of the error energy budget. The first author is grateful for encouraging and supporting discussions with Dr. Jie Liang. This research is supported by the National Science Foundation under AGS Grants 1114849

and 1305798. Computing is performed at the Texas Advanced Computing Center.

APPENDIX A

Initial Moisture Field

The initial moisture field in our model setup is based on Tan et al. (2004), with only slight modification. The x-independent relative humidity profile for the MOIST case is given by

$$\mathrm{RH}(y,z)=\mathrm{RH}_0R(y)\begin{cases}1-0.9\left(\dfrac{z}{z_{\mathrm{rh}}}\right)^{\delta} & z<z_{\mathrm{rh}}\\ 0.1 & z\geq z_{\mathrm{rh}}\end{cases}\quad\text{and} \tag{A1}$$

$$R(y)=\begin{cases}R_1 & y\leq y_1\\ R_1+\dfrac{y-y_1}{y-y_2}(R_2-R_1) & y_1<y<y_2\\ R_2 & y\geq y_2\end{cases}, \tag{A2}$$

where $\mathrm{RH}_0=75$, $R_2=1$, $R_1=0.66$; $y_1=0.4y_c$, $y_2=0.9y_c$, $y_c=4000$ km; $z_{\mathrm{rh}}=8000$ km; and $\delta=1.25$.

For the RH50 case, the relative humidity is further reduced to half of its initial value.

APPENDIX B

DKE Budget Equation for Different Scale

The derivation of the DKE budget equation is adapted from Zhang et al. (2007) and Peng et al. (2014). As in Zhang et al. (2007), the difference momentum equations can be written as

$$\frac{\partial\delta u}{\partial t}=-\delta\left(\mathbf{u}\cdot\nabla_h u+w\frac{\partial u}{\partial z}\right)-\delta\left(\frac{1}{\rho}\frac{\partial p'}{\partial x}\right)+f\delta v+\delta D_u \tag{B1}$$

and

$$\frac{\partial\delta v}{\partial t}=-\delta\left(\mathbf{u}\cdot\nabla_h v+w\frac{\partial v}{\partial z}\right)-\delta\left(\frac{1}{\rho}\frac{\partial p'}{\partial y}\right)-f\delta u+\delta D_v. \tag{B2}$$

Note δD terms include not only the diffusion but also the large-scale damping effect due to planetary boundary layer scheme and the Rayleigh damping effect at the model top.

Multiply Eqs. (B1) and (B2) by $\overline{\rho}\delta u$ and $\overline{\rho}\delta v$, respectively, then take the sum, and we get

$$\frac{\partial}{\partial t}(\mathrm{DKE})=\left[-\overline{\rho}(\delta u)\delta\left(\mathbf{u}\cdot\nabla_h u+w\frac{\partial u}{\partial z}\right)-\overline{\rho}(\delta v)\delta\left(\mathbf{u}\cdot\nabla_h v+w\frac{\partial v}{\partial z}\right)\right]+\left[-\overline{\rho}(\delta u)\delta\left(\frac{1}{\rho}\frac{\partial p'}{\partial x}\right)-\overline{\rho(\delta v)\delta\left(\frac{1}{\rho}\frac{\partial p'}{\partial y}\right)}\right]+\mathrm{Damping}. \tag{B3}$$

Here DKE is defined as $\mathrm{DKE}=(1/2)\overline{\rho}[(\delta u)^2+(\delta v)^2]$.

In our analysis, we separate the budget into three different scale ranges (large scale or L, wavelength $>$ 1000 km; intermediate scale or M, 1000 km $>$ wavelength $>$ 200 km; small scale or S, wavelength $<$ 200 km). Since the DKE budget equations for different scales are similar, here we only show the derivations for the large-scale (L) budget equation.

Use a large-scale filter for each term in (B1) and (B2), we have

$$\frac{\partial(\delta u)_L}{\partial t}=-\delta\left(\mathbf{u}\cdot\nabla_h u+w\frac{\partial u}{\partial z}\right)_L-\delta\left(\frac{1}{\rho}\frac{\partial p'}{\partial x}\right)_L+f(\delta v)_L+\delta(D_u)_L\quad\text{and} \tag{B4}$$

$$\frac{\partial(\delta v)_L}{\partial t}=-\delta\left(\mathbf{u}\cdot\nabla_h v+w\frac{\partial v}{\partial z}\right)_L-\delta\left(\frac{1}{\rho}\frac{\partial p'}{\partial y}\right)_L-f(\delta u)_L+\delta(D_v)_L. \tag{B5}$$

Again, multiplying Eqs. (B4) and (B5) by $\overline{\rho}(\delta u)_L$ and $\overline{\rho}(\delta v)_L$, respectively, we get the budget equation for large-scale DKE [Eq. (3) in the text]:

$$\frac{\partial}{\partial t}(\mathrm{DKE})_L=\left[-\overline{\rho}(\delta u)_L\delta\left(\mathbf{u}\cdot\nabla_h u+w\frac{\partial u}{\partial z}\right)_L-\overline{\rho}(\delta v)_L\delta\left(\mathbf{u}\cdot\nabla_h v+w\frac{\partial v}{\partial z}\right)_L\right]+\left[-\overline{\rho}(\delta u)_L\delta\left(\frac{1}{\rho}\frac{\partial p'}{\partial x}\right)_L-\overline{\rho}(\delta v)_L\delta\left(\frac{1}{\rho}\frac{\partial p'}{\partial y}\right)_L\right]+(\mathrm{Damping})_L. \tag{B6}$$

Note here is $(\mathrm{DKE})_L$ defined as in $(\mathrm{DKE})_L = (1/2)\overline{\rho}[(\delta u)_L^2 + (\delta v)_L^2]$.

APPENDIX C

Decomposition of the Pressure Term in the DKE Budget Equation

a. Cross-scale contribution of the pressure term

Unlike the nonlinear advection term, the pressure term in the budget equation derived above does not have a contribution across the scale ranges. The proof is listed below. We can divide the density into two parts (mean and perturbation), $\rho = \overline{\rho} + \rho'$, assuming $\rho' \ll \overline{\rho}$, then

$$\delta\left(\frac{1}{\rho}\frac{\partial p'}{\partial x}\right) \sim \delta\left(\frac{1}{\overline{\rho}}\frac{\partial p'}{\partial x}\right) \sim \frac{1}{\overline{\rho}}\delta\left(\frac{\partial p'}{\partial x}\right). \tag{C1}$$

The first part of the pressure term then becomes

$$-\overline{\rho}\delta u\delta\left(\frac{1}{\rho}\frac{\partial p'}{\partial x}\right) \sim -\overline{\rho}\delta u\frac{1}{\overline{\rho}}\delta\left(\frac{\partial p'}{\partial x}\right) = \delta u\delta\left(\frac{\partial p'}{\partial x}\right). \tag{C2}$$

Thus, the cross-scale contribution of the pressure term should be

$$-\overline{\rho}(\delta u)_l\delta\left(\frac{1}{\rho}\frac{\partial p'}{\partial x}\right)_m \sim (\delta u)_l\delta\left(\frac{\partial p'}{\partial x}\right)_m \to A\sin(lx)B\sin(mx), \tag{C3}$$

where l and m represent different wavenumbers and wavelengths and A and B are the amplitudes. Note that we need to integrate the pressure term over the whole domain to consider its total contribution. According to the orthogonality of the Fourier expansion, the integration equals zero, which means that the pressure term does not have any cross-scale contribution. The nonlinear advection term is the only term that is responsible for the redistribution of the energy across different scales.

b. Decomposition of the pressure term

The pressure term can be further decomposed as follows:

$$\begin{aligned}\text{Pressure term} &= -\overline{\rho}\delta u\delta\left(\frac{1}{\rho}\frac{\partial p'}{\partial x}\right) - \overline{\rho}\delta v\delta\left(\frac{1}{\rho}\frac{\partial p'}{\partial y}\right)\\ &\sim -\delta u\delta\left(\frac{\partial p'}{\partial x}\right) - \delta v\delta\left(\frac{1}{\rho}\frac{\partial p'}{\partial y}\right)\\ &= -\delta\mathbf{u}\cdot\delta(\nabla p')\\ &\sim -\delta\mathbf{u}\cdot\delta(C_p\theta_v\overline{\rho}\nabla\pi'),\end{aligned} \tag{C4}$$

where $\pi = (p/p_0)^{R_d/C_p}$ is the Exner pressure, $\pi' = \pi - \overline{\pi}$, $\theta_v = \theta(1 + 0.61q_v)$ is the virtual potential temperature, and C_p is the specific heat of the dry air at constant pressure.

Using integration by part, we have

$$\begin{aligned}\text{Pressure term} &\sim -\delta\mathbf{u}\cdot\delta(C_p\theta_v\overline{\rho}\nabla\pi')\\ &\sim -C_p\theta_v\overline{\rho}\delta\mathbf{u}\cdot\delta(\nabla\pi')\\ &= -C_p\theta_v\overline{\rho}\delta\mathbf{u}\cdot\nabla(\delta\pi')\\ &= -C_p\theta_v\overline{\rho}\{\nabla\cdot[(\delta\mathbf{u})(\delta\pi')] - (\delta\pi')\delta(\nabla\cdot\mathbf{u})\}\\ &= C_p\theta_v\overline{\rho}[(\delta\pi')\delta(\nabla\cdot\mathbf{u})].\end{aligned} \tag{C5}$$

Note the first term in the brackets $\nabla\cdot[(\delta\mathbf{u})(\delta\pi')]$ becomes zero after integrating over the whole domain as a result of the idealized boundary conditions in our simulation.

Using the pseudo-incompressible equation for moist air [Eq. (A11) of Peng et al. (2014)],

$$\nabla\cdot\mathbf{u} = \frac{H_m}{\overline{\theta}} - \frac{1}{\overline{\rho}\,\overline{\theta}}\frac{\partial(\overline{\rho}\,\overline{\theta}w)}{\partial z}. \tag{C6}$$

We have

$$\begin{aligned}\text{Pressure term} &\sim C_p\theta_v\overline{\rho}[(\delta\pi')\delta(\nabla\cdot\mathbf{u})]\\ &= C_p\theta_v\overline{\rho}\left\{(\delta\pi')\delta\left[\frac{H_m}{\overline{\theta}} - \frac{1}{\overline{\rho}\,\overline{\theta}}\frac{\partial(\overline{\rho}\,\overline{\theta}w)}{\partial z}\right]\right\}\\ &\sim C_p\overline{\rho}(\delta\pi')\delta H_m - C_p\delta\pi'\frac{\partial[\overline{\rho}\,\overline{\theta}(\delta w)]}{\partial z}\\ &= C_p\overline{\rho}(\delta\pi')\delta H_m - C_p\frac{\partial[\overline{\rho}\,\overline{\theta}(\delta\pi')(\delta w)]}{\partial z} + C_p\overline{\rho}\,\overline{\theta}(\delta w)\frac{\partial(\delta\pi')}{\partial z}.\end{aligned} \tag{C7}$$

The first term represents the direct influence of the diabatic heating. This term is very small. The second term is the convergence of the difference vertical pressure flux, which corresponds to the gravity wave flux to the first order. Note, if integrated over the entire domain, then this term should be close to 0. The last term is the difference buoyancy flux, which represents the conversion of potential energy to horizontal kinetic

energy; this is the dominant contribution term in this study.

Since the pressure term does not have a cross-scale effect, as is shown in (C1), the decomposition of pressure term for different scale is the same and will not be shown here.

REFERENCES

Bei, N., and F. Zhang, 2007: Impacts of initial condition errors on mesoscale predictability of heavy precipitation along the Mei-Yu front of China. *Quart. J. Roy. Meteor. Soc.*, **133**, 83–99, doi:10.1002/qj.20.

——, and ——, 2014: Mesoscale predictability of moist baroclinic waves: Variable and scale-dependent error growth. *Adv. Atmos. Sci.*, **31**, 995–1008, doi:10.1007/s00376-014-3191-7.

Callies, J., R. Ferrari, and O. Buhler, 2014: Transition from geostrophic turbulence to inertia–gravity waves in the atmospheric energy spectrum. *Proc. Natl. Acad. Sci. USA*, **111**, 17 033–17 038, doi:10.1073/pnas.1410772111.

Davis, C. A., and K. A. Emanuel, 1991: Potential vorticity diagnosis of cyclogenesis. *Mon. Wea. Rev.*, **119**, 1929–1952, doi:10.1175/1520-0493(1991)119<1929:PVDOC>2.0.CO;2.

Durran, D., and M. Gingrich, 2014: Atmospheric predictability: Why butterflies are not of practical importance. *J. Atmos. Sci.*, **71**, 2476–2488, doi:10.1175/JAS-D-14-0007.1.

Hohenegger, C., and C. Schär, 2007: Predictability and error growth dynamics in cloud resolving models. *J. Atmos. Sci.*, **64**, 4467–4478, doi:10.1175/2007JAS2143.1.

Hong, S.-Y., and H.-L. Pan, 1996: Nonlocal boundary layer vertical diffusion in a medium-range forecast model. *Mon. Wea. Rev.*, **124**, 2322–2339, doi:10.1175/1520-0493(1996)124<2322:NBLVDI>2.0.CO;2.

Klemp, J. B., J. Dudhia, and A. D. Hassiotis, 2008: An upper gravity-wave absorbing layer for NWP applications. *Mon. Wea. Rev.*, **136**, 3987–4004, doi:10.1175/2008MWR2596.1.

Lin, Y.-L., R. D. Farley, and H. D. Orville, 1983: Bulk parameterization of the snow field in a cloud model. *J. Climate Appl. Meteor.*, **22**, 1065–1092, doi:10.1175/1520-0450(1983)022<1065:BPOTSF>2.0.CO;2.

Lorenz, E. N., 1969: Atmospheric predictability as revealed by naturally occurring analogues. *J. Atmos. Sci.*, **26**, 636–646, doi:10.1175/1520-0469(1969)26<636:APARBN>2.0.CO;2.

——, 1982: Atmospheric predictability experiments with a large numerical model. *Tellus*, **34**, 505–513, doi:10.1111/j.2153-3490.1982.tb01839.x.

——, 1996: Predictability—A problem partly solved. *Proc. Seminar on Predictability*, Reading, United Kingdom, ECMWF, 1–18.

Mapes, B., S. Tulich, T. Nasuno, and M. Satoh, 2008: Predictability aspects of global aqua-planet simulations with explicit convection. *J. Meteor. Soc. Japan*, **86A**, 175–185, doi:10.2151/jmsj.86A.175.

Melhauser, C., and F. Zhang, 2012: Practical and intrinsic predictability of severe and convective weather at the mesoscales. *J. Atmos. Sci.*, **69**, 3350–3371, doi:10.1175/JAS-D-11-0315.1.

Morss, R. E., C. Snyder, and R. Rotunno, 2009: Spectra, spatial scales, and predictability in a quasigeostrophic model. *J. Atmos. Sci.*, **66**, 3115–3130, doi:10.1175/2009JAS3057.1.

Nastrom, G. D., and K. S. Gage, 1985: A climatology of atmospheric wavenumber spectra of wind and temperature observed by commercial aircraft. *J. Atmos. Sci.*, **42**, 950–960, doi:10.1175/1520-0469(1985)042<0950:ACOAWS>2.0.CO;2.

Palmer, T. N., A. Döring, and G. Seregin, 2014: The real butterfly effect. *Nonlinearity*, **27**, R123–R141, doi:10.1088/0951-7715/27/9/R123.

Peng, J., L. Zhang, Y. Luo, and Y. Zhang, 2014: Mesoscale energy spectra of the mei-yu front system. Part I: Kinetic energy spectra. *J. Atmos. Sci.*, **71**, 37–55, doi:10.1175/JAS-D-13-085.1.

Plougonven, R., and C. Snyder, 2007: Inertia–gravity waves spontaneously generated by jets and fronts. Part I: Different baroclinic life cycles. *J. Atmos. Sci.*, **64**, 2502–2520, doi:10.1175/JAS3953.1.

Rodwell, M. J., and Coauthors, 2013: Characteristics of occasional poor medium-range weather forecasts for Europe. *Bull. Amer. Meteor. Soc.*, **94**, 1393–1405, doi:10.1175/BAMS-D-12-00099.1.

Rotunno, R., and C. Snyder, 2008: A generalization of Lorenz's model for the predictability of flows with many scales of motion. *J. Atmos. Sci.*, **65**, 1063–1076, doi:10.1175/2007JAS2449.1.

Selz, T., and G. C. Craig, 2015a: Upscale error growth in a high-resolution simulation of a summertime weather event over Europe. *Mon. Wea. Rev.*, **143**, 813–827, doi:10.1175/MWR-D-14-00140.1.

——, and ——, 2015b: Simulation of upscale error growth with a stochastic convection scheme. *Geophys. Res. Lett.*, **42**, 3056–3062, doi:10.1002/2015GL063525.

Simmons, A. J., and B. J. Hoskins, 1978: The life cycles of some nonlinear baroclinic waves. *J. Atmos. Sci.*, **35**, 414–432, doi:10.1175/1520-0469(1978)035<0414:TLCOSN>2.0.CO;2.

Skamarock, W. C., and Coauthors, 2008: A description of the Advanced Research WRF version 3. NCAR Tech. Note NCAR/TN-475+STR, 113 pp., doi:10.5065/D68S4MVH.

Tan, Z.-M., F. Zhang, R. Rotunno, and C. Snyder, 2004: Mesoscale predictability of moist baroclinic waves: Experiments with parameterized convection. *J. Atmos. Sci.*, **61**, 1794–1804, doi:10.1175/1520-0469(2004)061<1794:MPOMBW>2.0.CO;2; Corrigendum, **65**, 1479, doi:10.1175/2007JAS2715.1.

Tao, D., and F. Zhang, 2014: Effect of environmental shear, sea-surface temperature, and ambient moisture on the formation and predictability of tropical cyclones: An ensemble-mean perspective. *J. Adv. Model. Earth Syst.*, **6**, 384–404, doi:10.1002/2014MS000314.

——, and ——, 2015: Effects of vertical wind shear on the predictability of tropical cyclones: Practical versus intrinsic limit. *J. Adv. Model. Earth Syst.*, **7**, 1534–1553, doi:10.1002/2015MS000474.

Taraphdar, S., P. Mukhopadhyay, R. L. Lueng, F. Zhang, S. Abhilash, and B. N. Goswami, 2014: The role of moist processes in the intrinsic predictability of Indian Ocean cyclones. *J. Geophys. Res. Atmos.*, **119**, 8032–8048, doi:10.1002/2013JD021265.

Thorncroft, C. D., B. J. Hoskins, and M. E. McIntyre, 1993: Two paradigms of baroclinic-wave life-cycle behaviour. *Quart. J. Roy. Meteor. Soc.*, **119**, 17–55, doi:10.1002/qj.49711950903.

Tribbia, J., and D. Baumhefner, 2004: Scale interactions and atmospheric predictability: An updated perspective. *Mon. Wea. Rev.*, **132**, 703–713, doi:10.1175/1520-0493(2004)132<0703:SIAAPA>2.0.CO;2.

Vallis, G. K., 2006: *Atmospheric and Oceanic Fluid Dynamics*. Cambridge University Press, 745 pp.

Waite, M. L., and C. Snyder, 2013: Mesoscale energy spectra of moist baroclinic waves. *J. Atmos. Sci.*, **70**, 1242–1256, doi:10.1175/JAS-D-11-0347.1.

Wei, J., and F. Zhang, 2014: Mesoscale gravity waves in moist baroclinic jet–front systems. *J. Atmos. Sci.*, **71**, 929–952, doi:10.1175/JAS-D-13-0171.1.

Zhang, F., 2004: Generation of mesoscale gravity waves in upper-tropospheric jet–front systems. *J. Atmos. Sci.*, **61**, 440–457, doi:10.1175/1520-0469(2004)061<0440:GOMGWI>2.0.CO;2.

——, and J. A. Sippel, 2009: Effects of moist convection on hurricane predictability. *J. Atmos. Sci.*, **66**, 1944–1961, doi:10.1175/2009JAS2824.1.

——, and D. Tao, 2013: Effects of vertical wind shear on the predictability of tropical cyclones. *J. Atmos. Sci.*, **70**, 975–983, doi:10.1175/JAS-D-12-0133.1.

——, C. Snyder, and R. Rotunno, 2002: Mesoscale predictability of the ''surprise'' snowstorm of 24–25 January 2000. *Mon. Wea. Rev.*, **130**, 1617–1632, doi:10.1175/1520-0493(2002)130<1617:MPOTSS>2.0.CO;2.

——, ——, and ——, 2003: Effects of moist convection on mesoscale predictability. *J. Atmos. Sci.*, **60**, 1173–1185, doi:10.1175/1520-0469(2003)060<1173:EOMCOM>2.0.CO;2.

——, A. M. Odins, and J. W. Nielsen-Gammon, 2006: Mesoscale predictability of an extreme warm-season precipitation event. *Wea. Forecasting*, **21**, 149–166, doi:10.1175/WAF909.1.

——, N. Bei, R. Rotunno, C. Snyder, and C. C. Epifanio, 2007: Mesoscale predictability of moist baroclinic waves: Convection-permitting experiments and multistage error growth dynamics. *J. Atmos. Sci.*, **64**, 3579–3594, doi:10.1175/JAS4028.1.

Zhang, Y., F. Zhang, Z. Meng, and D. J. Stensrud, 2015: Predictability of the 20 May 2013 tornadic thunderstorm event in Oklahoma: Sensitivity to synoptic timing and topographical forcing. *Mon. Wea. Rev.*, **143**, 2973–2997, doi:10.1175/MWR-D-14-00394.1.

——, ——, ——, and ——, 2016: Intrinsic predictability of the 20 May 2013 tornadic thunderstorm event in Oklahoma at storm scales. *Mon. Wea. Rev.*, doi:10.1175/MWR-D-15-0105.1, in press.

Zhu, H., and A. Thorpe, 2006: Predictability of extratropical cyclones: The influence of initial condition and model uncertainties. *J. Atmos. Sci.*, **63**, 1483–1497, doi:10.1175/JAS3688.1.